Delayed Hopf bifurcations in reaction-diffusion systems in two space dimensions

Ryan Goh, * Tasso J. Kaper, † Theodore Vo ‡

November 18, 2024

Abstract

For multi-scale differential equations (or fast-slow equations), one often encounters problems in which a key system parameter slowly passes through a bifurcation. In this article, we show that a pair of prototypical reaction-diffusion equations in two space dimensions can exhibit delayed Hopf bifurcations. Solutions that approach attracting/stable states before the instantaneous Hopf point stay near these states for long, spatially-dependent times after these states have become repelling/unstable. We use the complex Ginzburg-Landau equation and the Brusselator models as prototypes. We show that there exist two-dimensional spatio-temporal buffer surfaces and memory surfaces in the three dimensional space-time, and we derive asymptotic formulas for them. At each point in the domain, these surfaces determine how long the delay in the loss of stability lasts, *i.e.,* to leading order when the spatially-dependent onset of the post-Hopf oscillations occurs. Also, the onset of the oscillations in these PDEs is a hard onset.

2020 MSC codes: 35B32, 35K57, 35B36, 37L10, 37G15
keywords: Slow passage through Hopf bifurcation, dynamic bifurcation, hard onset of oscillations, spatio-temporal buffer surface, spatio-temporal memory surface, stationary phase method, steepest descents method, complex Ginzburg-Landau equation, Brusselator model

*Department of Mathematics and Statistics, Boston University, Boston, MA 02215, USA mailto:rgoh@math.bu.edu

†Department of Mathematics and Statistics, Boston University, Boston, MA 02215, USA mailto:tasso@math.bu.edu

‡School of Mathematics, Monash University, Clayton, Victoria 3800, Australia mailto:theodore.vo@monash.edu

1 Introduction

Many systems of multi-scale differential equations undergo dynamic Hopf bifurcations in which a parameter slowly changes and a stable state becomes unstable due to the slow, generic passage of a pair of eigenvalues through the imaginary axis. When the governing equations in the multi-scale (or fast-slow) systems are analytic ordinary differential equations (ODEs), it has been known for over 50 years that there are delays in the onset of the instabilities [4, 16, 21, 36, 37, 38, 39, 40, 46, 47, 48, 49]. Solutions which have approached the stable (attracting) states before the instantaneous Hopf bifurcations remain near those states long after they have become unstable (repelling) in the dynamic Hopf bifurcations. This phenomenon is known as delayed Hopf bifurcation (DHB).

The dynamic manifestation of DHB is that the onset of the post-Hopf oscillations is a hard onset, with the systems transitioning rapidly to large scale oscillations when they leave neighborhoods of the unstable states. This contrasts with the gradual square root growth of the oscillation amplitudes in generic classical Hopf bifurcations.

Applications of DHB in ODE models have been studied in many areas of science and engineering: chemistry [8, 16, 29, 30, 47], electrical circuits [20, 23, 50], electrocardiac models [31], fluid mechanics and geophysics [2, 14, 22, 33], mechanical oscillators [11, 39], neuroscience [4, 5, 9, 10, 25, 43, 44, 48], economics [19], among others. For each of these models, the long delay between the instantaneous bifurcation and the onset of oscillations, which is $\mathcal{O}(1/\varepsilon)$ in the fast time (where ε is the small parameter measuring the time-scale separation), plays an important role in the system dynamics.

Recently, it has been shown that the DHB phenomenon occurs not only in analytic ODEs but also naturally in one-dimensional, multi-scale partial differential equations (PDEs) of reaction-diffusion type [18, 26]. As a parameter slowly varies, these systems undergo dynamic super-critical Hopf bifurcations. Examples studied in [18, 26] include the complex Ginzburg-Landau equation, the FitzHigh-Nagumo PDE, and the Hodgkin-Huxley PDE. Additional theory for problems with spectral gaps is given in [3].

In this article, we show that the phenomenon of DHB also occurs in a pair of multi-scale reaction-diffusion PDEs in two space dimensions (2-D). In particular, we study DHB in the complex Ginzburg-Landau (CGL) PDE in 2-D and in the Brusselator model in 2-D. Both of these equations have Hopf bifurcations in which an attracting quasi-steady state (QSS) becomes a repelling QSS, and we consider the problems in which the bifurcation parameters slowly and generically pass through the Hopf points.

First, we use asymptotic analysis on the linearized CGL PDE in 2-D to

show that solutions that approach the attracting QSS before the instantaneous Hopf bifurcation remain close to it even after it has become repelling in the Hopf bifurcation. From the asymptotic analysis, we find that the delays between the time of the instantaneous Hopf bifurcation and the onset of the post-Hopf oscillations are long ($\mathcal{O}(1/\varepsilon)$ in the fast time) and generally spatially-dependent.

Next, we quantify the duration of these delays. We define spatio-temporal buffer surfaces and spatio-temporal memory surfaces in the three-dimensional space-time of the CGL PDE. These are the surfaces along which the amplitudes of the particular and homogeneous solutions of the linearised CGL PDE, respectively, cross a threshold, and cause the solution of the full PDE to diverge from the repelling QSS. We derive asymptotic formulas for both surfaces, and we determine how they depend on the initial data and on the properties of the sources terms in the CGL PDE. We find that, at each point $(\mathfrak{x}, \mathfrak{y})$ in the domain, numerically-computed solutions of the fully nonlinear CGL PDE with initial data given at $\mu_0 < 0$ stay close to the repelling QSS until they reach the spatio-temporal memory surface or the spatio-temporal buffer surface, whichever occurs first at that point. Hence, the linear terms appear to drive the phenomena of DHB in these PDEs, just as they do in the analytic ODEs.

Finally, we present numerical simulations showing that DHB also occurs in the Brusselator PDE model in 2-D. Since its creation [42], the Brusselator has served as a prototypical model in pattern formation and chemical oscillation theory (see for example [15]). Here, we consider the case when the main bifurcation parameter slowly passes through the Hopf point. As with the CGL PDE, solutions of the Brusselator PDE that approach the attracting QSS before the instantaneous Hopf bifurcation remain near the QSS for long times after it has become repelling. We find that there is a substantial –and generally point-dependent– delay before the onset of oscillations occurs.

The asymptotic and numerical results we present here for these prototypical pattern-forming systems in 2-D extend our earlier work for DHB in PDEs in 1-D [18, 26]. In particular, in [18] we defined buffer curves and memory curves for the linearized CGL PDE in 1-D and derived asymptotic formulas for their spatio-temporal dependence. We showed that key terms in the particular solution are exponentially small up until the spatio-temporal buffer curve, and precisely along it these terms become $\mathcal{O}(1)$. Similarly, the homogeneous solution is exponentially small up until the memory curve and large after that. Overall, for the CGL PDE in 1-D, we showed that there is a competition between these exponentially small terms: at each point in the 1-D domain the term that ceases being small first determines the length of the delay to leading order at that point, and hence also when the hard

onset of the (post-Hopf) oscillations occurs. The memory and buffer surfaces defined in this article play a similar role for the CGL PDE in 2-D.

We recall that classical Hopf bifurcations are ubiquitous in PDEs and spatially extended systems in 2-D. General results are presented, for example, in [45]. Some specific examples include electrodeposition models [32], bulk-surface reaction-diffusion [41], and nematic liquid crystals [12, 13], in addition to the CGL and Brusselator models studied here.

This article is organized as follows. In Section 2, we present the main asymptotic analysis to show that DHB occurs in the linearized CGL equation with a slowly varying parameter in two space dimensions. In Section 3, we derive the asymptotic formulas for the spatio-temporal buffer surface and the memory surface for the CGL PDE. In Section 4, we present the results of numerical simulations for the fully nonlinear CGL equation that complement the theoretical predictions (of the previous two sections) for the spatio-temporal dependence of the delayed Hopf bifurcations. Section 5 features the DHB results obtained from numerical simulations of the Brusselator model in 2-D. Conclusions are presented in Section 6. Some asymptotic calculations are presented in the Appendix.

2 Analysis of DHB in the 2-D CGL equation

In two space dimensions, the CGL equation with a source term and a slowly varying parameter is given by

$$\begin{aligned} A_t &= (\mu + i\omega_0)A - (1 + i\alpha)|A|^2 A + \sqrt{\varepsilon} I_a(x, y) + \varepsilon d\Delta A, \\ \mu_t &= \varepsilon. \end{aligned} \tag{1}$$

Here, $(x, y) \in \mathbf{R}^2$, $\Delta = \frac{\partial^2}{\partial x^2} + \frac{\partial^2}{\partial y^2}$, $t \geqslant 0$, $A = A(x, y, t)$ is complex-valued, and $0 < \varepsilon \ll 1$ is a small parameter. The linear growth rate $\mu = \mu(t)$ is real for the main phenomena we study. The other system parameters satisfy $\omega_0 > 0$, α is real, d may be complex-valued ($d = d_R + id_I$) with $d_R > 0$, and these parameters are all independent of ε. The source term $I_a(x, y)$ breaks the symmetry $A \to Ae^{i\theta}$ for any real θ of the CGL equation and is taken to be bounded and positive, with uniformly bounded derivatives. The initial data at $\mu(0) = \mu_0 < 0$ is $A(x, y, 0) = A_0(x, y)$, and taken to be bounded and continuous for all (x, y). We refer to [1] for the classical CGL PDE.

2.1 The attracting and repelling quasi-steady states

The PDE (1) has an attracting quasi-steady state (QSS) for all $\mu < -\delta$, where $\delta > 0$ is small and $\mathcal{O}(1)$ with respect to ε, and solutions approach it

at an exponential rate. Similarly, it has a repelling QSS for all $\mu > \delta$, from which solutions diverge at an exponential rate. These QSS are given by

$$\begin{aligned} A_{QSS}(x,\mu) = &-\sqrt{\varepsilon}\frac{I_a(x,y)}{\mu+i\omega_0} \\ &+ \varepsilon^{\frac{3}{2}}\left(\frac{I_a(x,y)+d(\mu+i\omega_0)\Delta I_a(x,y)}{(\mu+i\omega_0)^3} - \frac{(1+i\alpha)I_a^3(x,y)}{(\mu+i\omega_0)^2(\mu^2+\omega_0^2)}\right) \\ &+ \mathcal{O}(\varepsilon^{\frac{5}{2}}). \end{aligned} \tag{2}$$

Here, the $\mathcal{O}(\varepsilon^{\frac{5}{2}})$ terms depend on (x,y) and μ.

2.2 Solution of the linearised equation

In this section, we consider $\mu_0 < 0$ and solve the linearised equation,

$$\begin{aligned} A_t &= (\mu+i\omega_0)A + \sqrt{\varepsilon}I_a(x,y) + \varepsilon d\Delta A, \\ \mu_t &= \varepsilon. \end{aligned} \tag{3}$$

This equation may be simplified using an integrating factor. Let $B(x,y,\mu) = A(x,y,\mu)e^{\frac{-(\mu+i\omega_0)^2}{2\varepsilon}}$. The equation for B is an inhomogeneous heat equation,

$$\sqrt{\varepsilon}B_\mu = \sqrt{\varepsilon}d\Delta B + I_a(x,y)e^{\frac{-(\mu+i\omega_0)^2}{2\varepsilon}}. \tag{4}$$

The solution of (4) with initial data $B(x,y,\mu_0) = A_0(x,y)e^{\frac{-(\mu_0+i\omega_0)^2}{2\varepsilon}}$ is obtained by superimposing the homogeneous solution $B_h(x,y,\mu)$ and the particular solution $B_p(x,y,\mu)$. For $\mu > \mu_0$, we find

$$B_h(x,y,\mu) = \frac{e^{\frac{-(\mu_0+i\omega_0)^2}{2\varepsilon}}}{4\pi d(\mu-\mu_0)}\int_{\mathbf{R}^2}\exp\left[\frac{-(x-x')^2-(y-y')^2}{4d(\mu-\mu_0)}\right]A_0(x',y')dx'dy'$$

Here, we have used the fundamental solution of the heat equation in two dimensions, $\Phi(x,y,\mu) = \frac{1}{4\pi d\mu}e^{\frac{-(x^2+y^2)}{4d\mu}}$. Also, for $\mu > \mu_0$,

$$\begin{aligned} B_p(x,y,\mu) &= \frac{1}{\sqrt{\varepsilon}}\int_{\mu_0}^{\mu} g(x,y,\mu-\tilde{\mu})e^{\frac{-(\tilde{\mu}+i\omega_0)^2}{2\varepsilon}}d\tilde{\mu}, \\ g(x,y,\mu) &= \frac{1}{4d\pi\mu}\int_{\mathbf{R}^2}\exp\left[\frac{-(x-x')^2-(y-y')^2}{4d\mu}\right]I_a(x',y')dx'dy' \end{aligned}$$

Transforming back to the original dependent variable using the integrating factor, we find that for $\mu > \mu_0$ the homogeneous solution is

$$A_h(x,y,\mu) = \frac{e^{\frac{1}{2\varepsilon}(\mu^2-\mu_0^2+2i\omega_0(\mu-\mu_0))}}{4\pi d(\mu-\mu_0)} \int_{\mathbf{R}^2} e^{\frac{-(x-x')^2-(y-y')^2}{4d(\mu-\mu_0)}} A_0(x',y')dx'dy'. \tag{5}$$

Furthermore, for $\mu > \mu_0$ the particular solution is

$$\begin{aligned} A_p(x,y,\mu) &= \frac{e^{\frac{(\mu+i\omega_0)^2}{2\varepsilon}}}{\sqrt{\varepsilon}} \int_{\mu_0}^{\mu} g(x,y,\mu-\tilde{\mu}) e^{\frac{-(\tilde{\mu}+i\omega_0)^2}{2\varepsilon}} d\tilde{\mu}, \\ g(x,y,\mu) &= \frac{1}{4\pi d\mu} \int_{\mathbf{R}^2} \exp\left[\frac{-(x-x')^2-(y-y')^2}{4d\mu}\right] I_a(x',y')dx'dy'. \end{aligned} \tag{6}$$

This completes the derivation of the solution of the linearised equation. We calculate A_h for several different types of initial data $A_0(x,y)$ in Section 3.1, and A_p for several different types of source terms in Section 3.2. Also, we observe here that it will be useful to distinguish between initial data $A_0(x,y,\mu_0)$ given for $\mu_0 \leqslant -\omega_0$ and for $-\omega_0 < \mu_0 < 0$.

2.3 Solutions stay near the repelling QSS at least until $\mu = \omega_0$

In this section, we consider solutions with $\mu_0 \leqslant -\omega_0$. We show that not only do the solutions of (1) with $\mu_0 \leqslant -\omega_0$ remain close to the attracting QSS until the time of the instantaneous Hopf bifurcation at $\mu = 0$, but after the parameter crosses the instantaneous Hopf bifurcation they remain close to the repelling QSS as well, at least until the time $\mu = +\omega_0$ at all points (x,y) for the functions $I_a(x,y)$ we consider.

We consider complex values of μ in a horizontal strip with mid-line on the real axis and of sufficient height (at least $3\omega_0$). This enables the use of classical methods of stationary phase and steepest descents, see for example [6, 27, 35], to calculate $A_p(x,y,\mu)$. We find, for $\delta \leqslant \mu \leqslant \omega_0$,

$$\begin{aligned} A_p(x,y,\mu) = &-\sqrt{\varepsilon}\frac{I_a(x,y)}{\mu+i\omega_0} + \varepsilon^{\frac{3}{2}}\left(\frac{I_a(x,y)+d(\mu+i\omega_0)\Delta I_a(x,y)}{(\mu+i\omega_0)^3}\right) \\ &+ \mathcal{O}\left(\frac{\varepsilon^{\frac{5}{2}}}{(\mu+i\omega_0)^5}\right) \\ &+ \left(\sqrt{2\pi}g(x,y,\mu+i\omega_0) + \mathcal{O}(\sqrt{\varepsilon})\right) e^{\frac{1}{2\varepsilon}(\mu+i\omega_0)^2}. \end{aligned} \tag{7}$$

The calculation is presented in Appendix A.

The first and second terms are precisely the leading order terms in the expansion of the repelling QSS for the linear CGL (cf. (2), where the QSSs are given for the cubic CGL equation). The third (remainder) term contains the higher order terms in the asymptotic expansion of the repelling QSS, and continued integration by parts will yield them. The fourth term is exponentially small for $\mu \in [\delta, \omega_0 - K\varepsilon^r)$, for some $K > 0$ and any $0 < r < 1$. It is a classic Stokes type term. This term is not in the expansion of the repelling QSS (on $\mu > \delta$) to all orders. Rather, it is beyond all orders, $\mathcal{O}\left(e^{-\frac{\omega_0^2}{2\varepsilon}}\right)$, arising naturally from tracking solutions on (and near) the attracting QSS along a contour over the saddle point in the complex μ plane and into the regime of $\mathrm{Re}(\mu) > 0$. It is a measure of the exponentially small distance between the attracting and repelling QSS at $\mu = 0$.

Overall, formula (7) shows that, at all points (x, y), the solutions of the linear CGL equation with Gevrey regular data $A_0(x)$ given at $\mu_0 \leqslant -\omega_0$ remain near the repelling QSS at least until $\mu = \omega_0$ to leading order.

Next, one needs to include also the nonlinear terms from (1). This was done for DHB in the 1-D CGL PDE in Section 6 of [18]. First, we used the same type of integrating factor (as used in (3) above) to rewrite the nonlinear PDE for $B(x, \mu)$ there. Then, we split the solution into two parts: $B(x, \mu) = B_p(x, \mu) + b(x, \mu)$, where we recall that B_p is the particular solution of the linearized equation. The PDE for the remainder term $b(x, \mu)$ was converted into an integral equation. We showed formally that there is a mild solution of that integral equation, using an iterative method, and that the magnitude of $b(x, \mu)$ remains small at least until $\mu = \omega_0$. Hence, the solution of the full nonlinear PDE remains near the repelling QSS at least until ω_0.

As the estimates of the mild formulation of the 1-D nonlinear equation only used $L^\infty \to L^\infty$ estimates for the heat semi-group, we expect that a similar formal analysis will hold for two spatial dimensions, as well. That is, based on decomposing $B(x, y, \mu) = B_p(x, y, \mu) + b(x, y, \mu)$, we expect that $b(x, y, \mu)$ remains small at least until μ reaches ω_0. Fundamentally, the nonlinear terms remain exponentially small at least as long as the linear terms do.

3 The spatio-temporal memory surface and spatio-temporal buffer surface for the CGL equation

In this section, we derive the general formulas for the spatio-temporal memory and buffer surfaces of (1), and we apply these to several classes of initial data $A_0(x, y)$ and several different source terms $I_a(x, y)$, respectively.

3.1 The spatio-temporal memory surface

By writing the homogeneous solution $A_h(x, y, \mu)$ as a single exponential function, we define the spatio-temporal memory surface to be the set of points $(x, y, \mu_{\text{mem}}(x, y))$ at which the real part of the argument of the exponential vanishes. In this section, we examine three different types of initial data: constant, Gaussian, and periodic, in order to study how the spatio-temporal memory surface depends on the functional form of $A_0(x, y)$.

For constant initial data $A_0(x, y) = 1$, one finds from (5) that

$$A_h(x, y, \mu) = e^{\frac{1}{2\varepsilon}(\mu^2 - \mu_0^2 + 2i\omega_0(\mu - \mu_0))}. \tag{8}$$

It is independent of (x, y). Hence, $A_h(x, y)$ is exponentially small for all $\mu \in (\mu_0, -\mu_0)$. At $\mu = -\mu_0$, the real part of the exponential vanishes, implying that the memory surface is a horizontal plane in the (x, y, μ) space:

$$\mu_{\text{mem}}(x, y) = -\mu_0, \quad \text{for all } (x, y), \tag{9}$$

where we recall $\mu_0 < 0$. Then, for $\mu > -\mu_0$, A_h becomes exponentially large.

For Gaussian initial data $A_0(x, y) = e^{\frac{-(x^2+y^2)}{4\sigma}}$, formula (5) shows that the homogeneous solution is given by

$$A_h(x, y, \mu) = \left[\frac{\sigma}{\sigma + d(\mu - \mu_0)}\right] e^{\frac{1}{2\varepsilon}(\mu^2 - \mu_0^2 + 2i\omega_0(\mu - \mu_0))} e^{\frac{-(x^2+y^2)}{4(\sigma + d(\mu - \mu_0))}}. \tag{10}$$

At each (x, y), the real part of the argument of the exponential vanishes for

$$\begin{aligned} \frac{\mu^2 - \mu_0^2}{2\varepsilon} + \ln(\sigma) - \frac{1}{2}\ln\left((\sigma + d_R(\mu - \mu_0))^2 + d_I^2(\mu - \mu_0)^2\right) \\ - \frac{(x^2 + y^2)(\sigma + d_R(\mu - \mu_0))}{4[(\sigma + d_R(\mu - \mu_0))^2 + d_I^2(\mu - \mu_0)^2]} = 0, \end{aligned} \tag{11}$$

where we recall $d = d_R + id_I$ in (1). Hence, to leading order asymptotically, we find that the spatio-temporal memory surface is parabolic in x and y,

$$\begin{aligned}\mu_{\text{mem}}(x,y) = |\mu_0| - \frac{\varepsilon}{|\mu_0|}\left(\ln(\sigma) - \frac{1}{2}\ln\left((\sigma + 2d_R|\mu_0|)^2 + 4d_I^2|\mu_0|^2\right)\right) \\ + \frac{\varepsilon}{4|\mu_0|}\left(\frac{(x^2+y^2)(\sigma + 2d_R|\mu_0|)}{(\sigma + 2d_R|\mu_0|)^2 + 4d_I^2|\mu_0|^2}\right) + \mathcal{O}(\varepsilon^2).\end{aligned} \tag{12}$$

For periodic initial data $A_0(x,y) = \cos\frac{\pi}{L}(x-y)\cos\frac{\pi}{L}(x+y)$, the homogeneous solution for $\mu > \mu_0$ is

$$A_h(x,y,\mu) = e^{\frac{1}{2\varepsilon}(\mu^2 - \mu_0^2 + 2i\omega_0(\mu-\mu_0))}e^{-\frac{4\pi^2 d(\mu-\mu_0)}{L^2}}\cos\tfrac{\pi}{L}(x-y)\cos\tfrac{\pi}{L}(x+y). \tag{13}$$

Hence, at any point (x,y), the real part of the argument vanishes for

$$\frac{1}{2\varepsilon}(\mu^2 - \mu_0^2) - \frac{4\pi^2 d(\mu-\mu_0)}{L^2} + \ln|\cos\tfrac{\pi}{L}(x-y)\cos\tfrac{\pi}{L}(x+y)| = 0. \tag{14}$$

Asymptotically to leading order, one finds logarithmic dependence on A_0,

$$\mu_{\text{mem}}(x,y) = |\mu_0| + \frac{8\varepsilon\pi^2 d}{L^2} - \frac{\varepsilon}{|\mu_0|}\ln|\cos\tfrac{\pi}{L}(x-y)\cos\tfrac{\pi}{L}(x+y)|. \tag{15}$$

These theoretical results for $\mu_{\text{mem}}(x,y)$ with constant, Gaussian, and periodic initial data are compared to simulations of (1) in Section 4.

Remark. In [18], for the CGL PDE in 1-D, we used the label homogeneous exit time curve. (There, homogeneous referred to the curve being defined by A_h, not that the curve is spatially homogeneous.) Here, we label it instead the spatio-temporal memory surface, since it is determined by the memory of the initial data. One could also label it the spatio-temporal way-in way-out surface, in analogy with the way-in way-out function defined for DHB in analytic ODEs [36, 37].

3.2 The spatio-temporal buffer surface

In this section, we focus on the particular solution $A_p(x,y,\mu)$ with special emphasis on the fourth (last) term in the general formula (7). We consider $\delta \leqslant \mu \leqslant \omega_0$ and label this term G:

$$G(x,y,\mu) = \left(\sqrt{2\pi}g(x,y,\mu+i\omega_0) + \mathcal{O}(\sqrt{\varepsilon})\right)e^{\frac{1}{2\varepsilon}(\mu+i\omega_0)^2}. \tag{16}$$

The function G is the component of the particular solution $A_p(x,y,\mu)$ that measures the deviation from the repelling QSS (where we recall that the first

three terms in (7) represent the QSS). It is generated by passage over the saddle point at $\mu = -i\omega_0$ in the complex μ-plane, as shown in App. A. It is present in all solutions that start from initial data at any $\mu_0 < 0$, including solutions on the attracting QSS.

The spatio-temporal buffer surface is defined as the surface along which

$$|G(x, y, \mu)| = 1, \tag{17}$$

to leading order. Here, we derive a general formula for the spatio-temporal buffer surface for smooth, bounded sources $I_a(x, y)$, and asymptotic formulas for it with constant, Gaussian, periodic, and stripe sources. We will see that G ceases to be exponentially small and becomes $\mathcal{O}(1)$ in a spatially-dependent manner, in general. This will imply that all solutions with initial data given at $\mu_0 < 0$, including those on the attracting QSS, must leave an $\mathcal{O}(1)$ neighborhood of the repelling QSS when μ reaches the buffer surface, irrespective of how large $|\mu_0|$ is, *i.e.,* irrespective of how far in the distant past the solutions approached the attracting QSS.

From (16), we find that the spatio-temporal buffer surface is given implicitly by

$$\mathrm{Re}\left[\ln\left(\sqrt{2\pi}g(x, y, \mu + i\omega_0)\right) + \frac{1}{2\varepsilon}(\mu + i\omega_0)^2\right] = 0, \tag{18}$$

for general smooth and bounded source terms $I_a(x, y)$. We label the solution $\mu_{\mathrm{buf}}(x, y)$. Its graph is the spatio-temporal buffer surface. To leading order,

$$\mu_{\mathrm{buf}}^2(x, y) = \omega_0^2 - \varepsilon \ln(2\pi) - 2\varepsilon \ln|g(x, y, \omega_0 + i\omega_0)|. \tag{19}$$

At each point (x, y), the buffer surface $\mu_{\mathrm{buf}}(x, y)$ determines the time at which the deviation of $A_p(x, y, \mu)$ from the repelling QSS ceases to be exponentially small.

We begin with constant source terms, $I_C(x, y) = c$, and set $c = 1$ without loss of generality. Substituting this into the integral for g in (6), we find

$$g(x, y, \mu - \tilde{\mu}) = 1, \quad \text{for all } (x, y) \text{ and } \mu > \tilde{\mu} \geqslant \mu_0. \tag{20}$$

Hence, by (19), the buffer surface is to leading order

$$\mu_{\mathrm{buf}}(x, y) = \omega_0 - \frac{\varepsilon}{2\omega_0} \ln(2\pi), \quad \text{for all } (x, y). \tag{21}$$

It is independent of (x, y). Hence, at all points in the domain, the particular solution ceases to be exponentially small uniformly at this time, μ_{buf}.

Next, we consider Gaussian source terms, $I_G(x,y) = e^{\frac{-(x^2+y^2)}{4\sigma}}$, with $\sigma > 0$. Using (6), we find

$$g(x,y,\mu-\tilde{\mu}) = \left(\frac{\sigma}{\sigma + d(\mu-\tilde{\mu})}\right) \exp\left[\frac{-(x^2+y^2)}{4(\sigma+d(\mu-\tilde{\mu}))}\right]. \tag{22}$$

Hence, (19) implies that, to leading order, the buffer surface is

$$\begin{aligned}\mu_{\text{buf}}(x,y) = \omega_0 &- \frac{\varepsilon}{2\omega_0}\ln\left(\frac{2\pi\sigma^2}{(\sigma+\omega_0(d_R-d_I))^2+\omega_0^2(d_R+d_I)^2}\right)\\ &+ \frac{\varepsilon}{4\omega_0}\left[\frac{(\sigma+\omega_0(d_R-d_I))}{(\sigma+\omega_0(d_R-d_I))^2+\omega_0^2(d_R+d_I)^2}\right](x^2+y^2).\end{aligned} \tag{23}$$

For periodic source terms, $I_P(x,y) = \cos\frac{\pi}{L}(x-y)\cos\frac{\pi}{L}(x+y)$, (6) yields

$$g(x,y,\mu-\tilde{\mu}) = e^{-4\pi^2 d(\mu-\tilde{\mu})/L^2}\cos\tfrac{\pi}{L}(x-y)\cos\tfrac{\pi}{L}(x+y). \tag{24}$$

Hence, (19) implies that, to leading order, the buffer surface is

$$\begin{aligned}\mu_{\text{buf}}(x,y) = \omega_0 &- \frac{\varepsilon}{2\omega_0}\ln(2\pi) + \frac{4\varepsilon\pi^2(d_R-d_I)}{L^2}\\ &- \frac{\varepsilon}{\omega_0}\ln|\cos\tfrac{\pi}{L}(x-y)\cos\tfrac{\pi}{L}(x+y)|.\end{aligned} \tag{25}$$

Finally, we let H denote the Heaviside step function (1 on $x > 0$ and 0 on $x < 0$) and study stripe source terms,

$$I_S(x,y) = \sum_k \left(H(x-x_k) - H(x-(x_k+h))\right). \tag{26}$$

Here, h is the width of the stripe, x_k denotes the left edge of the k-th stripe, and $x_{k+1} - x_k = \Delta > h$ for each k. We use (6) to derive

$$g(x,y,\mu-\tilde{\mu}) = \frac{1}{2}\sum_k \left(\operatorname{erf}\left(\frac{x_k+h-x}{\sqrt{4d(\mu-\tilde{\mu})}}\right) - \operatorname{erf}\left(\frac{x_k-x}{\sqrt{4d(\mu-\tilde{\mu})}}\right)\right) \tag{27}$$

where $\operatorname{erf} z = \frac{2}{\sqrt{\pi}}\int_0^z e^{-t^2}\,dt$ is the error function. Hence, (19) implies that, to leading order, the buffer surface is given by

$$\mu_{\text{buf}}(x,y) = \omega_0 - \frac{\varepsilon}{2\omega_0}\ln(2\pi) - \frac{\varepsilon}{\omega_0}\ln|g(x,y,\omega_0(1+i))|, \tag{28}$$

where g is given by (27). For these source terms, the spatio-temporal buffer surface is compared to the numerical solutions of the PDE (1) in Section 4.

4 DHB in the CGL equation with constant, Gaussian, and stripe sources

In this section, we report on the spatially-dependent duration of the delayed Hopf bifurcation (DHB) observed in direct numerical simulations of solutions of the CGL PDE (1) with $\mu_0 < 0$. We will examine both cases in which the initial time satisfies $\mu_0 \in (-\omega_0, 0)$ and $\mu_0 \leqslant -\omega_0$. We recall that the escape surface is the graph of the time $\mu_{\text{esc}}(x, y)$ in (x, y, μ) space. Numerically, we obtain $\mu_{\text{esc}}(x, y)$ by calculating the set of points at which $|\text{Re}(A_{\text{num}}(x, y)) - \text{Re}(A_{\text{QSS}}(x, y))| = \delta_{\text{th}}$, where $A_{\text{num}}(x, y)$ is the numerically computed solution of (1), $A_{\text{QSS}}(x, y)$ is the value of A along the QSS (2), and δ_{th} denotes a threshold.

We will show that $\mu_{\text{esc}}(x, y)$ agrees with the predictions made from the memory and buffer surfaces. At each point (x, y),

$$\mu_{\text{esc}}(x, y) \approx \min(\mu_{\text{mem}}(x, y), \mu_{\text{buf}}(x, y)). \tag{29}$$

We work with several different types of source terms (constant, Gaussian, and stripe) and with the asymptotic expansions for these surfaces derived in Section 3.

In the numerical simulations, we used symmetric Strang splitting [34], with centered finite differences for the spatial discretisation and 4th order Runge-Kutta with fixed time step for the time discretisation. The results were also checked independently using a Chebyshev grid for the spatial discretisation, finding good agreement.

4.1 DHB with constant source term

In the first representative simulation, we study DHB in (1) with constant source term $I_C(x, y) = 1$ and Gaussian initial data,

$$A_0(x, y) = c_1 + c_2 e^{-\frac{x^2+y^2}{4\sigma}}, \quad c_1, c_2 > 0, \tag{30}$$

given at $\mu_0 = -0.3$, which we note is in $(-\omega_0, 0)$. We show the escape surface in Fig. 1(a). Below it, *i.e.,* for all $\mathcal{O}(1)$ values $\mu < \mu_{\text{esc}}(x, y)$, the solution is near the repelling QSS. Then, just before μ reaches it, oscillations of amplitude $\mathcal{O}(\sqrt{\varepsilon})$ set in at (x, y). Furthermore, as soon as μ is slightly beyond $\mu_{\text{esc}}(x, y)$, the amplitude of the oscillations at (x, y) is large.

We observe that the delayed, post-Hopf, temporal oscillations first set in at the origin of the domain, at the vertex of the paraboloid-type surface, quite close to $\mu = -\mu_0$. As μ slowly increases past $-\mu_0$, the oscillations

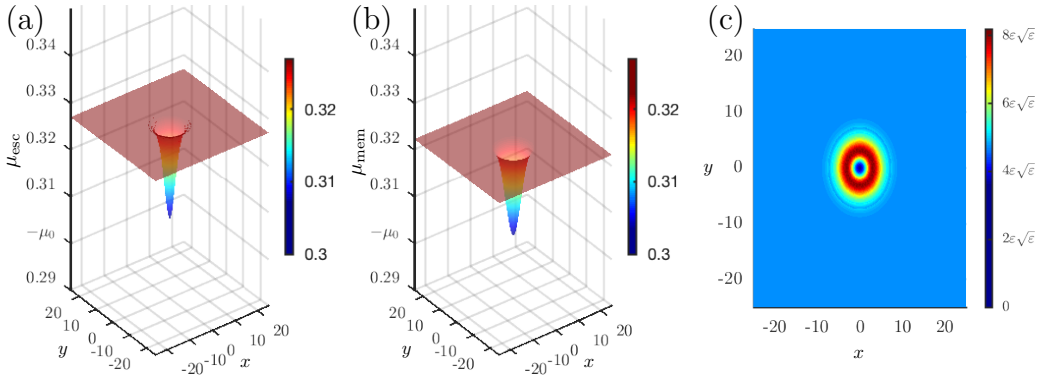

Figure 1: (a) In the three-dimensional (x, y, μ) space, the surface $\mu_{esc}(x, y)$ is where the hard onset of the oscillations occurs. It has been obtained from direct numerical simulation of the PDE (1) with constant source term $I_C(x, y) = 1$ and Gaussian initial data $A_0(x, y) = c_1 + c_2 e^{\frac{-x^2+y^2}{4\sigma}}$ with $(c_1, c_2, \sigma) = (0.5, 0.5, 2.5)$, given at $\mu_0 = -0.3$. (b) The memory surface $\mu_{mem}(x, y)$ is given by (11). It gives the leading order asymptotics of the escape time for all (x, y). (c) The difference $|\mu_{esc}(x, y) - \mu_{mem}(x, y)|$ is shown in the projection onto the (x, y) plane. Here, the parameters are $d = 1$, $\omega_0 = 0.5$, $\alpha = 0.2$, and $\varepsilon = 0.01$.

occur on successively larger disks about the origin. Then, once μ reaches 0.327 approximately, there is a fairly rapid transition, and the oscillations occur on the entire domain.

For comparison, we show the memory surface $\mu_{mem}(x, y)$ in Fig. 1(b). The memory surface was computed as follows. First, we combined the homogeneous solutions (8) and (10) to determine the homogeneous solution, A_h, with the initial data (30), $A_0(x, y) = c_1 + c_2 e^{\frac{-x^2+y^2}{4\sigma}}$. Then, by enforcing the condition $|A_h| = 1$, we obtain the leading order asymptotic relation

$$\mu^2 - \mu_0^2 + 2\varepsilon \ln \left| c_1 + c_2 \frac{\sigma}{\sigma + d(\mu - \mu_0)} \exp\left(\frac{-(x^2 + y^2)}{4(\sigma + d(\mu - \mu_0))} \right) \right| = 0 \quad (31)$$

for the memory surface corresponding to this A_0.

The difference $|\mu_{esc}(x, y) - \mu_{mem}(x, y)|$ is shown in Fig. 1(c). At the center of the Gaussian, the difference is small (with magnitude of approximately 10^{-5}, *i.e.*, $\mathcal{O}(\varepsilon^{5/2})$). Then, in an annular region about the origin (red and dark red), the difference is slightly larger, due to nonlinear effects. Finally, both surfaces exhibit a fairly rapid transition into the regime (blue region in Fig. 1(c), red in (a) and (b)) where they are essentially constant, since the Gaussian is tiny. Here, $\mu_{mem}(x, y) = \sqrt{\mu_0^2 - 2\varepsilon \ln c_1} \approx 0.322$ to leading order

(as obtained from (31) for large $x^2 + y^2$), which agrees well with the value observed numerically in (1).

Moreover, for the CGL with this (constant) source term, the buffer surface lies above the memory surface for all (x, y) in 3-D, since $\mu_{\rm buf}(x, y) = \sqrt{\omega_0^2 - \varepsilon \ln(2\pi)} \approx 0.481$ for all (x, y). Hence, for all (x, y), the minimum in $\mu_{\rm esc}(x, y) \sim \min\{\mu_{\rm mem}(x, y), \mu_{\rm buf}(x, y)\}$ is given entirely by the memory surface in this simulation.

The second representative simulation is also with $I_C(x, y) = 1$. However, now the initial data given at $-\omega_0 < \mu_0 < 0$ is periodic,

$$A_0(x, y) = p_1 + p_2 \cos \frac{\pi}{L}(x - y) \cos \frac{\pi}{L}(x + y), \tag{32}$$

with $p_1 > p_2 > 0$, so that $A_0(x, y)$ is strictly positive everywhere. The results are shown in Fig. 2.

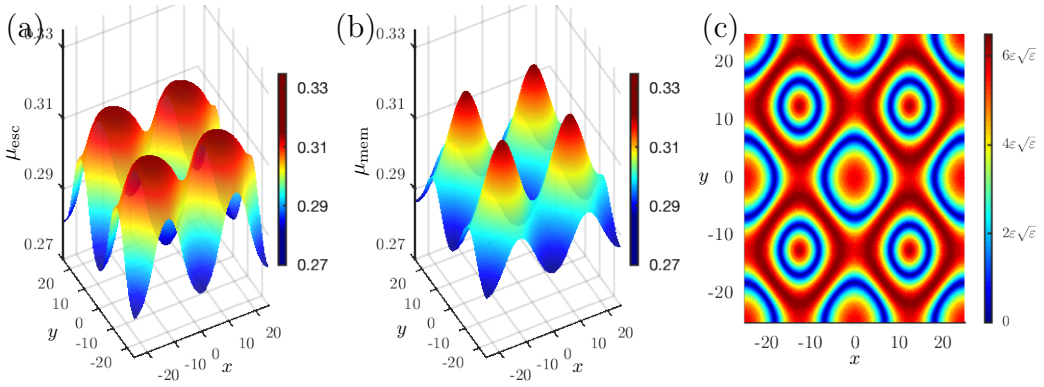

Figure 2: (a) In the three dimensional (x, y, μ) space, the surface $\mu_{\rm esc}(x, y)$ is where the hard onset of the oscillations occurs. It has been obtained from direct simulation of (1) with constant source term $I_C(x, y) = 1$ and periodic initial data $A_0(x, y) = p_1 + p_2 \cos \frac{\pi}{L}(x - y) \cos \frac{\pi}{L}(x + y)$ at $\mu_0 = -0.3$ with $(p_1, p_2, L) = (1, 0.5, 25)$. (b) The memory surface $\mu_{\rm mem}(x, y)$ given by (14). (c) The surface $|\mu_{\rm num}(x, y) - \mu_{\rm mem}(x, y)|$ shown in the projection onto the (x, y) plane. The parameters are $d = 1, \omega_0 = 0.5$, $\alpha = 0.2$, and $\varepsilon = 0.01$.

The escape surface computed from the numerical simulations (Fig. 2(a)) shows that the oscillations first occur at time $\mu \approx 0.281$ at the points $(x, y) = (j_1 L, j_2 L)$, where $j_1, j_2 = -1, 0, 1$ (dark blue), *i.e.*, at the maxima of $A_0(x, y)$ where $\cos \frac{\pi}{L}(x - y) \cos \frac{\pi}{L}(x + y) = 1$. About each of those points, the oscillations set in on successively larger disks as μ slowly increases, until those disks collide at $\mu \approx 0.306$ (near the transition from yellow to orange). Then, as μ increases further, the escape surface consists of the four inverted

paraboloid segments (orange and red). The peaks occur at time $\mu \approx 0.315$ at the points $(x, y) = \left(\frac{j_1 L}{2}, \frac{j_2 L}{2}\right)$, where $j_1, j_2 = -1, 1$ (dark red), *i.e.*, at the minima of $A_0(x, y)$ where $\cos\frac{\pi}{L}(x-y)\cos\frac{\pi}{L}(x+y) = -1$.

For comparison, the memory surface $\mu_{\text{mem}}(x, y)$ is defined by

$$\mu^2 - \mu_0^2 + 2\varepsilon \ln\left|p_1 + p_2 \exp\left(-\frac{4\pi^2 d(\mu-\mu_0)}{L^2}\right)\cos\tfrac{\pi}{L}(x-y)\cos\tfrac{\pi}{L}(x+y)\right| = 0, \tag{33}$$

and shown in Fig. 2(b). It has global minima (dark blue) when $\mu_{\text{mem}} = \sqrt{|\mu_0|^2 - 2\varepsilon \ln\left(1 + 0.5e^{\frac{-8\pi^2 d|\mu_0|}{L^2}}\right)} \approx 0.2866$ to leading order, with $\mu_0 = -0.3$. These occur at the points where $A_0(x, y)$ has its maxima. Also, the memory surface has global maxima (dark red) when $\mu \approx 0.3211$, at the points where $A_0(x, y)$ has its minima. In between, it has the same conical shape qualitatively as the escape surface.

The difference between $\mu_{\text{esc}}(x, y)$ and $\mu_{\text{mem}}(x, y)$ is shown in Fig. 2(c). The nonlinear terms cause μ_{esc} to grow more steeply from the local minima, compared to the memory surface, so that the disks collide at a slightly later time than for the memory surface. Then, after the disks collide, the inverted paraboloids are slightly wider in $\mu_{\text{esc}}(x, y)$ due to the nonlinear terms.

Finally, for this second representative simulation, we report that the buffer surface also lies above the memory surface for all (x, y) in 3-D. Indeed, with constant source $I_C(x, y) = 1$, $\mu_{\text{buf}}(x, y) = \sqrt{\omega_0^2 - \varepsilon \ln(2\pi)} \approx 0.481$. Hence, also here the minimum is given by the memory surface for all (x, y).

Remark. In the second simulation, we also combined two homogeneous solutions, here (8) and (13), to determine the homogeneous solution A_h that corresponds to the periodic initial profile $A_0(x, y) = p_1 + p_2 \cos\frac{\pi}{L}(x - y)\cos\frac{\pi}{L}(x + y)$. Then, by setting $|A_h| = 1$, we obtain (33).

Remark. We also explored the effect of giving the initial data at different times, including $\mu_0 < -\omega_0$, while keeping the source term and initial data the same as in the second simulation. In these simulations (data not shown), we observe that $\mu_{\text{esc}}(x, y) = \omega_0 - \varepsilon \ln(2\pi)$ to leading order for all (x, y), as determined by A_p, recall (21). This is as expected from the analysis, because $\mu_{\mathbf{buf}}(x, y) < \mu_{\text{mem}}(x, y)$ at all points when the initial data is given at time $\mu_0 < -\omega_0$ and ε is sufficiently small.

4.2 DHB with Gaussian source term

Gaussian source terms can be used to model spatially localized, radially symmetric inputs, such as a circular spot of visible light that shines on the

reactor in a chemical pattern-forming experiment. A representative example of (1) with Gaussian source term is shown in Fig. 3. Here, $I_G(x,y) = \exp\left(-\frac{x^2+y^2}{4\sigma}\right)$ with $\sigma = 1$, and the initial data at $\mu_0 = -0.75$ is $A_0(x,y) = \cos\frac{\pi}{L}(x-y)\cos\frac{\pi}{L}(x+y)$ with $L = 25$.

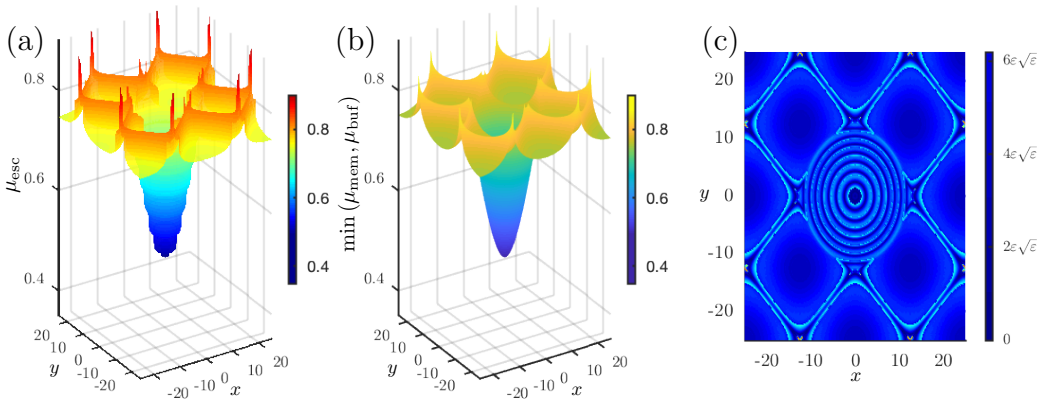

Figure 3: (a) In the three dimensional (x,y,μ) space, the surface $\mu_{esc}(x,y)$ is where the hard onset of the oscillations occurs. It has been obtained from direct simulation of (1) with Gaussian source term $I_G(x,y) = \exp\left(-\frac{x^2+y^2}{4\sigma}\right)$ and periodic initial data $A_0(x,y) = \cos\frac{\pi}{L}(x-y)\cos\frac{\pi}{L}(x+y)$ at $\mu_0 = -0.75$ with $L = 25$. (b) The predicted escape surface is given by the minimum of $\mu_{buf}(x,y)$ (parabolic part) and $\mu_{mem}(x,y)$ (periodic part). (c) The surface $|\mu_{esc}(x,y) - \min\{\mu_{mem}, \mu_{buf}\}|$ shown in the projection onto the (x,y) plane. The parameters are $d = 1, \omega_0 = 0.5$, $\alpha = 0.2$, and $\varepsilon = 0.01$.

From direct numerical simulations of the PDE, we find that the domain of the escape surface (Fig. 3(a)) can be split into two distinct parts: the annular region $R_G = \{(x,y) : x^2 + y^2 \leqslant 11.5^2\}$ and its complement $R_P = \mathbb{R}^2 \backslash R_G$. On R_G, the earliest numerically detected escape occurs at the origin for $\mu \approx 0.4905$. The escape surface is radially symmetric and increases on concentric rings, thus creating a rotationally-symmetric paraboloid. In contrast, for $(x,y) \in R_P$, the escape surface is no longer radially symmetric, and is instead a periodic tile pattern, reflecting the initial data. The minima occur at $\mu \approx 0.738$ (yellow/green regions) and the maxima at $\mu \approx 0.812$ (red lines between yellow/green regions).

For this source term and initial condition, the buffer surface is given by (23) and the memory surface is given by (14). In Fig. 3(b), we plot $\min\{\mu_{buf}(x,y), \mu_{mem}(x,y)\}$. On R_G, the minimum is given by the buffer surface, whereas it is given by the memory surface on R_P. The buffer surface predicts that the earliest onset occurs at the origin at $\mu \approx 0.4908$. The values

of μ_{buf} increase in a radially symmetric fashion until $\mu \approx -\mu_0 = 0.75$ on the boundary of R_G. Then, for (x, y) on R_P, the memory surface predicts the onset. (Compare Figs. 3(a) and (b).)

The difference $|\mu_{\text{esc}}(x, y) - \min\{\mu_{\text{buf}}(x, y), \mu_{\text{mem}}(x, y)\}|$ is small throughout, as shown in Fig. 3(c). The difference is especially small (of the order of the neglected terms in the asymptotic expansion) near the onset at the origin, which is at the minimum of the buffer surface, and also near the local minima of the memory surface.

4.3 DHB with stripe source term

Stripe source terms are also of fundamental interest. For example, chemical reactions irradiated with constant intensity light filtered through stripe masks can produce complex patterns, see [7, 17] and references within.

Here, we use a simple model for a strictly positive stripe source term,

$$I_S(x, y) = 1 + \frac{1}{2} \sum_{k=-2}^{2} \left(H(x - x_k) - H(x - (x_k + h)) \right), \tag{34}$$

where h is the stripe width, x_k denotes the left edge of the k-th stripe, and $x_{k+1} - x_k = \Delta > h$. We set $x_0 = -1.25$, $h = 2.5$, and $\Delta = 10$.

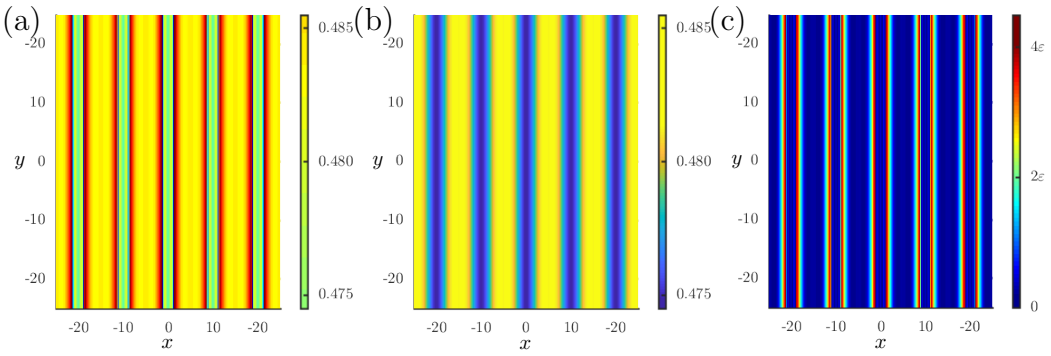

Figure 4: (a) The surface $\mu_{\text{esc}}(x, y)$, shown here in the projection onto the (x, y) plane, is where the hard onset of oscillations occurs. It has been obtained from numerical simulation of (1) with stripe source term $I_S(x, y)$ (34) and constant initial data $A_0(x, y) = 1$ given at $\mu_0 = -1$. (b) The buffer surface $\mu_{\text{buf}}(x, y)$ defined by (19), with g given by the linear combination of (20) and (27). (c) The difference $|\mu_{\text{esc}}(x, y) - \mu_{\text{buf}}(x, y)|$. The parameters are $d = 1, \omega_0 = 0.5$, $\alpha = 0.2$, and $\varepsilon = 0.01$.

For the PDE (1), the surfaces $\mu_{\text{esc}}(x, y)$ (calculated from direct numerical simulations) and $\mu_{\text{buf}}(x, y)$ (calculated from (20) and (27)) are shown in

Fig. 4(a) and (b), along with the difference in Fig. 4(c). From the plot of $\mu_{\text{esc}}(x, y)$, we see that the hard onset of oscillations occurs first at the points where $I_S(x, y)$ has its maximum, *i.e.,* inside the stripes. See the green stripes in the plot of $\mu_{\text{esc}}(x, y)$ in Fig. 4(a). The buffer curve $\mu_{\text{buf}}(x, y)$ also has local minima inside the stripes (blue stripes in Fig. 4(b)), and these stripes have approximately the same width as those of the escape surface. The difference in the green and blue stripes is of $\mathcal{O}(\varepsilon\sqrt{\varepsilon})$.

In the complementary regions, the PDE simulations show that the duration of the DHB is longer. The escape surface lies just below ω_0, by about 2ε (see the yellow stripes in Fig. 4(a)). In the complementary regions, the buffer surface transitions more gradually to its local maxima, which also occur at the local minima of the source term. Here, the difference is of $\mathcal{O}(\varepsilon\sqrt{\varepsilon})$.

The narrow red strips between the green and yellow bands in Fig. 4(a) correspond to the regions where the Heaviside function has a discontinuity. This discontinuity is smoothed out in the predicted buffer surface Fig. 4(b), so that $\mu_{\text{buf}}(x, y)$ is smooth and continuous across the whole domain. This difference is highlighted in Fig. 4(c). There, the error is small and of $\mathcal{O}(\varepsilon\sqrt{\varepsilon})$ throughout the blue regions, and is of $\mathcal{O}(\varepsilon)$ in the thin strips where the Heaviside function has jump discontinuities.

We add that, in this simulation with the stripe source term (34) and the constant initial data given at $\mu_0 = -1$, the memory surface (9) lies well above the buffer surface (21) for all (x, y). Hence, the escape time is determined exclusively by the buffer surface, as reported.

4.4 The competition between $\mu_{\text{mem}}(x, y)$ and $\mu_{\text{buf}}(x, y)$

In the above simulations, we have shown that at each point (x, y), $\mu_{\text{esc}}(x, y) \sim \min(\mu_{\text{mem}}(x, y), \mu_{\text{buf}}(x, y))$ to leading order. Therefore, in effect, there is a competition at every point (x, y) between $A_h(x, y, \mu)$ and $A_p(x, y, \mu)$ in which the first one that ceases being exponentially small determines the maximal duration of the delay in the Hopf bifurcation to leading order.

The memory surface $\mu_{\text{mem}}(x, y)$ depends to leading order on the initial time μ_0. Then, at $\mathcal{O}(\varepsilon)$, it also depends on the logarithm of $|A_h(x, y; \mu)|$. Recall, for example, (9), (12), and (15).

The space time buffer surface $\mu_{\text{buf}}(x, y)$ (recall (19) in Sec. 3.2) is determined to leading order by ω_0, which is the frequency at the instantaneous Hopf bifurcation, and then at $\mathcal{O}(\varepsilon)$ by the logarithm of the Stokes term $g(x, y, \omega_0(1 + i))$ in (19). Indeed, as highlighted by the analysis in the complex μ plane in Appendix A, the Stokes line through the saddle point at $\mu = -i\omega_0$ crosses the negative μ-axis at $\mu = -\omega_0$ (see Fig. 6). Hence, the initial time μ_0 is to the left of that here, and the contour used to find

$A_p(x, y, \mu)$ for values of $\mu > 0$ goes through that saddle. The saddle point method (applied in App. A) shows that the function $G(x, y, \mu)$ given by (16) arises due to passage over the saddle at $-i\omega_0$. For each $\mu > 0$, $G(x, y, \mu)$ measures the deviation of the solution A_p from the repelling QSS. On $\mu > 0$, it stays exponentially small at least until μ reaches $+\omega_0$, where the other Stokes line through the saddle reaches the positive μ-axis. Then, as μ slowly increases beyond ω_0, $G(x, y, \mu)$ ceases to be exponentially small –and grows to become $\mathcal{O}(1)$– in a spatially-dependent manner. That is why the buffer surface is defined by (19), *i.e.,* by when and where $|G| = 1$.

Therefore, at $\mathcal{O}(1)$, μ_0 and ω_0 determine the competition, and at $\mathcal{O}(\varepsilon)$ it is determined by the logarithmic terms. Moreover, for any finite value of ε, there can be a changeover between the two terms for which one wins the competition, since in general the logarithmic terms in both expressions can grow due to their spatial dependence. (See for example Fig. 3.)

5 DHB in the 2-D Brusselator model

In two space dimensions, the Brusselator model with a source term and a slowly varying rate constant is given by the following system:

$$\begin{aligned} u_t &= a(x, y) - (1 + b)u + u^2 v + \varepsilon d_u \Delta u, \\ v_t &= bu - u^2 v + \varepsilon d_v \Delta v, \\ b_t &= \varepsilon. \end{aligned} \tag{35}$$

Here, the independent variables are $(x, y) \in \mathbf{R}^2$ and $t \geqslant 0$, $\Delta = \frac{\partial^2}{\partial x^2} + \frac{\partial^2}{\partial y^2}$, and the subscript t denotes the partial derivative on t. The dependent variable u denotes the concentration of the activator chemical, and v that of the inhibitor species. The small parameter $0 < \varepsilon \ll 1$ measures the separation in the time scales. The spatially-dependent source term, $a(x, y)$, is taken to be positive, bounded, $\mathcal{O}(1)$ with respect to ε, and smooth. The parameter $b > 0$ denotes a rate constant that slowly increases in time, and $d_u, d_v > 0$ are the diffusivities of the activator and inhibitor.

5.1 Hopf bifurcation of the quasi-steady state

The Brusselator PDE (35) has a quasi-steady state (QSS),

$$u_{QSS}(x,y) = a(x,y) + \varepsilon\Delta\left(d_u a(x,y) + d_v\frac{b}{a(x,y)}\right) + \mathcal{O}(\varepsilon^2)$$
$$v_{QSS}(x,y) = \frac{b}{a(x,y)} + \frac{\varepsilon}{a^2(x,y)}\Delta\left((1-b)\frac{d_v b}{a(x,y)} - b d_u a(x,y)\right) + \mathcal{O}(\varepsilon^2). \tag{36}$$

We perform a linear stability analysis about the QSS by setting $u = u_{QSS} + \hat{u}$ and $v = v_{QSS} + \hat{v}$. The linearized system for $\hat{u}$ and $\hat{v}$ is

$$\begin{bmatrix} \hat{u}_t \\ \hat{v}_t \end{bmatrix} = M \begin{bmatrix} \hat{u} \\ \hat{v} \end{bmatrix} + \varepsilon \begin{bmatrix} d_u & 0 \\ 0 & d_v \end{bmatrix} \begin{bmatrix} \Delta\hat{u} \\ \Delta\hat{v} \end{bmatrix},$$

where

$$M = \begin{bmatrix} 2u_{QSS}v_{QSS} - (1+b) & u_{QSS}^2 \\ b - 2u_{QSS}v_{QSS} & -u_{QSS}^2 \end{bmatrix}.$$

Hence, by setting $\mathrm{Tr}(M) = 0$, we find that the PDE (35) exhibits a spatially-dependent Hopf bifurcation at $b = b_H(x,y)$, where

$$b_H(x,y) = \frac{1 + a^2 + 2\varepsilon a d_u \Delta a + \mathcal{O}(\varepsilon^2)}{1 + 2\varepsilon d_v \frac{1-a^2}{a}\Delta\frac{1}{a} + \mathcal{O}(\varepsilon^2)}, \tag{37}$$

and we have written a for $a(x,y)$. At each point $(x,y) \in \mathbf{R}^2$, the QSS is linearly stable for $b < b_H(x,y)$, and linearly unstable for $b > b_H(x,y)$. Moreover, the frequency, ω_H, at b_H is $\omega_H = a(x,y) + \mathcal{O}(\varepsilon)$.

Remark. The Brusselator model (35) exhibits (super-critical) Turing bifurcations. For example, with source $a(x,y) = a_0 + \varepsilon a_1(x,y) + \mathcal{O}(\varepsilon^2)$, where $a_0 > 0$ and $\mathcal{O}(1)$, Turing bifurcations occur at $b_T = \left(1 \pm \sqrt{\frac{d_u}{d_v}}a_0\right)^2 + \mathcal{O}(\varepsilon)$. The homogeneous state bifurcates into a spatially periodic state. The parameter values we have studied here were chosen so that the Turing bifurcations do not impact the DHB phenomenon. We think it would be interesting also to study the interactions between the two bifurcations.

5.2 Spatio-temporal dependence of the delayed Hopf bifurcations in the Brusselator model

In this section, we present the results of numerical simulations showing the spatio-temporal dependence of the delayed Hopf bifurcations (DHB) in the

Brusselator model (35). We take the initial value $b(t_0) < b_H(x,y)$ for all (x,y), so that the system slowly passes through the Hopf bifurcation $b_H(x,y)$ as b slowly increases, recall (37). We work primarily with a stripe source term,

$$a_S(x,y) = 1 + \varepsilon\alpha \sum_k \left(H(x - x_k) - H(x - (x_k + h))\right), \tag{38}$$

where $\alpha > 0$, x_k denotes the left edge of the k-th stripe, $x_{k+1} - x_k = \Delta$, $h < \Delta$ is the width of the stripe, and the stripes are sufficiently well-separated.

In each of the simulations we carried out, the solutions rapidly approach the attracting QSS for $b < b_H(x,y)$ and then, after the instantaneous Hopf point is crossed, they stay near the repelling QSS for long times, of $O(1/\varepsilon)$ duration in the fast time t. This is the delay in the Hopf bifurcation, and the solutions leave a neighborhood of the QSS in a spatially-dependent manner. Moreover, they do so by making a large rapid jump away from it, so that there is a hard onset of large-amplitude oscillations.

For the representative simulation shown in Fig. 5, we set $\alpha = 5$, $h = 0.1$, $x_0 = -0.05$, and $\Delta = 0.3$. The initial data is spatially periodic

$$u_0(x,y) = a(x,y) + \varepsilon \sin(\pi y(3x-2)), \quad v_0(x,t) = \tfrac{b_0}{a(x,y)} + \varepsilon \cos(\pi^2 xy). \tag{39}$$

The initial value of the parameter is $b_0 = b(t_0) = 1.5$ (see Fig. 5(a)), which is below the Hopf point $b = 2$ here. As the parameter b slowly increases, the solution rapidly approaches the attracting QSS, and the component of the solution given by the spatially periodic initial data decreases. By the time $b = 1.7$, the remnant of the initial data is faint (see Fig. 5(b)). Then, when b reaches $b = 2$, where the instantaneous Hopf bifurcation happens in (35), there is no visible trace of the initial data (see Fig. 5(c)).

As b continues to increase, the solution remains near the repelling QSS (see Fig. 5(d), where $b = 2.2$). It is not until $b = 2.4$ that small amplitude temporal (post-Hopf) oscillations begin to set in (see Fig. 5(e)). Also, the solution has regained a significant component given by the shape of the initial data. The oscillations rapidly become large amplitude oscillations when b reaches larger values (see Fig. 5(f)-(h), where $b = 2.6$, $b = 2.8$, $b = 3.0$, resp., and we note the changes in the vertical scales), and hence the observed onset is a hard onset. Also, by this time, there is significant interaction between the components coming from the initial data and the stripe source.

Further increases in b result in spatio-temporal patterns, such as the formation of spiral waves (see Fig. 5(i)). These spatial patterns arise from the interaction of the oscillations (which occur beyond the memory surface), the stripe source, and the diffusion.

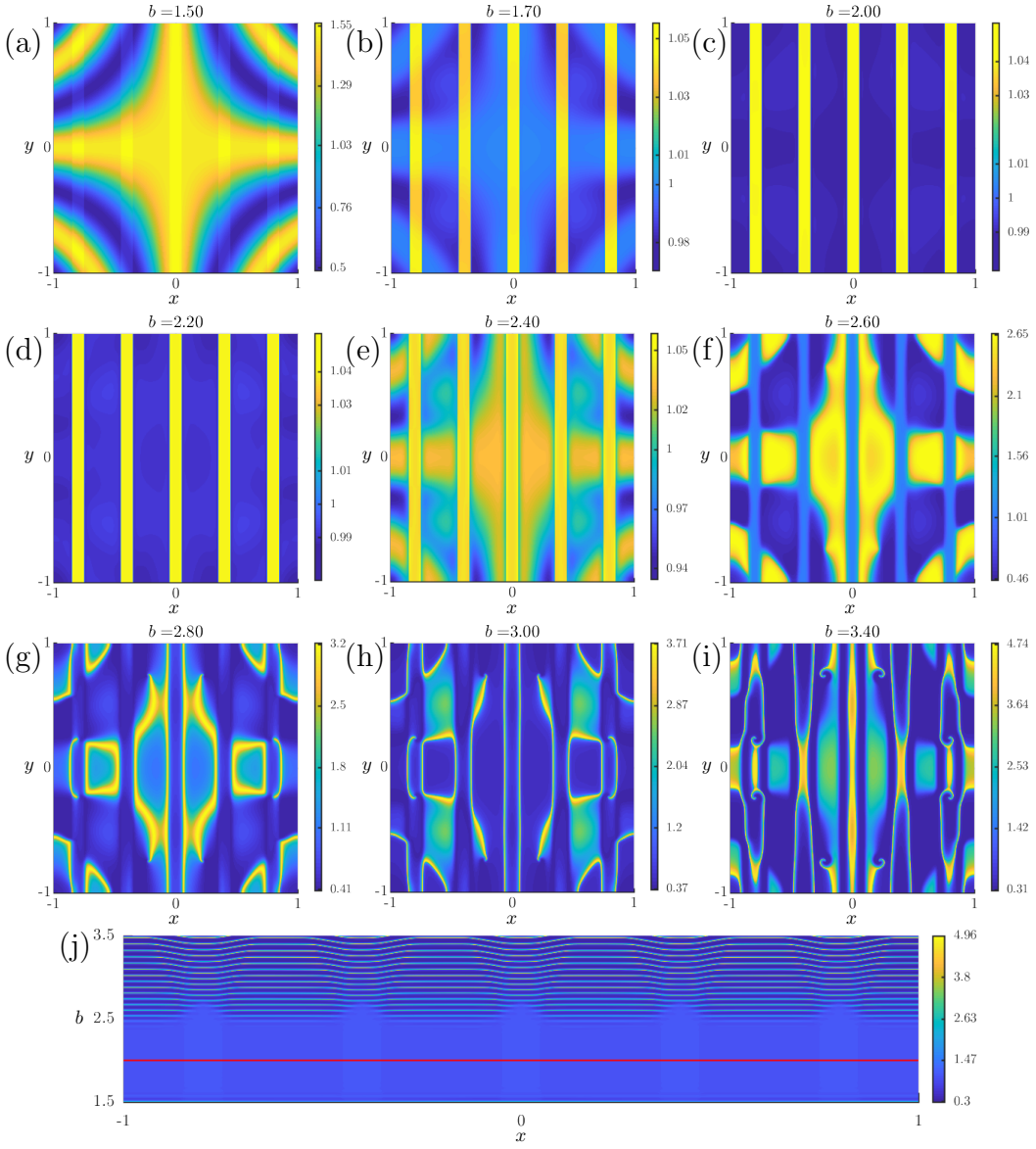

Figure 5: DHB in the 2-D Brusselator with stripe source (38) and spatially periodic initial data (39) given at $\mathtt{b}(\mathtt{t}_0) = 1.5$. Panels (a)–(i): the solution $\mathtt{u}(\mathtt{x}, \mathtt{y})$ rapidly converges to the source-dependent QSS, stays close to the QSS well-beyond the instantaneous HB at $\mathtt{b} = 2$, and exhibits a hard transition to oscillations. Note the different axes on (a)-(i). Panel (j): space-time evolution along $\mathtt{y} = 0$. The parameters are $\varepsilon = 0.01$, $\mathtt{d}_\mathtt{u} = 1 \times 10^{-3}$, $\mathtt{d}_\mathtt{v} = 5 \times 10^{-4}$, $\alpha = 5$, $\mathtt{h} = 0.1$, $\mathtt{x}_0 = -0.05$, and $\Delta = \mathtt{x}_{\mathtt{k}+1} - \mathtt{x}_\mathtt{k} = 0.4$.

A cross-section through $y = 0$ is shown in Fig. 5(j). The space-time plot shows that the solution stays close to the QSS (blue state) well past the instantaneous HB (red line) and the large-amplitude oscillations do not set in until $b \approx 2.5$. Cross-sections taken at other values of y are qualitatively the same, with some slight shifts in x.

Overall, we find that these primary features of DHB in the 2-D Brusselator –the long, spatially-dependent DHB and the hard, spatially-dependent onset of large-amplitude oscillations– are the same as those observed for DHB in the CGL PDE in 2-D (Section 4), as well as for DHB in PDEs in 1-D [3, 18, 26], in analytic ODEs [4, 16, 21, 36, 37, 38, 39, 40, 46, 48, 49], and in the applications cited in the Introduction.

6 Conclusions

In this article, we studied a pair of prototypical pattern-forming PDEs in two space dimensions. In both, an attracting quasi-steady state (QSS) becomes a repelling QSS as a key parameter varies slowly in time through a generic, super-critical Hopf bifurcation. We reported on the discovery of delayed Hopf bifurcations (DHB) in which solutions of these PDEs in 2-D stay near the (post-Hopf) repelling QSS for long, spatially-dependent periods of time ($\mathcal{O}(1/\varepsilon)$ fast time), before the spatially-dependent hard onset of large-amplitude oscillations occurs.

First, we generalized the asymptotic and numerical results of [18] for DHB in the CGL PDE in one space dimension to two dimensions. We introduced the spatio-temporal memory surface $\mu_{\rm mem}(x, y)$ and the spatio-temporal buffer surface $\mu_{\rm buf}(x, y)$, and we derived asymptotic formulas for them in the CGL PDE (recall Sections 3.1 and 3.2). These are the 2-D analogs of the 1-D memory and buffer curves introduced in [18].

The memory surface $\mu_{\rm mem}(x, y)$ is determined by when the homogeneous solution of the linearized equation reaches amplitude one, and hence stops being exponentially small. It is labeled the memory surface for the following reason: While the memory of the initial data fades quickly after the initial time $\mu_0 < 0$, because the solution rapidly (exponentially in time) approaches the attracting QSS before the instantaneous Hopf bifurcation, the memory of it is not lost. On the contrary, the component of the solution given by the initial data re-emerges (or resurges) in a spatially-dependent manner at $\mu_{\rm mem}(x, y)$ to leading order. The asymptotic formula for $\mu_{\rm mem}(x, y)$ quantifies its dependence on μ_0 and on the spatial structure of the general bounded, smooth, initial data $A_0(x, y)$. We applied it to several structurally different types of data (see (9), (12), and (15)).

The buffer surface $\mu_{\text{buf}}(x, y)$ is determined from the particular solution $A_p(x, y, \mu)$ by when $|G| = 1$, recall (17). It plays a central role in the dynamics of solutions for which initial data $A_0(x, y)$ is given at $\mu_0 \leqslant -\omega_0$. In particular, to leading order, all solutions with initial data given at $\mu_0 \leqslant -\omega_0$, including those on the attracting QSS, leave an $\mathcal{O}(1)$ neighborhood of the repelling QSS when μ reaches the buffer surface, irrespective of how large $|\mu_0|$ is, *i.e.,* irrespective of far in the distant past the solutions approached the attracting QSS. Furthermore, we derived the asymptotic formula for $\mu_{\text{buf}}(x, y)$, finding its dependence on the frequency ω_0 at the Hopf point and on the spatial structure of general, smooth, bounded source terms. Also, we applied the general formula to the cases of constant, Gaussian, periodic, and stripe sources, see (21), (23), (25), and (28).

Overall, for solutions of the CGL PDE (1) with initial data given at $\mu_0 < 0$, we found that the spatially-dependent duration of the DHB is given by $\mu_{\text{esc}}(x, y) = \min\{\mu_{\text{mem}}(x, y), \mu_{\text{buf}}(x, y)\}$ to leading order. Also, we found that there is good quantitative agreement between the asymptotic formulas for $\mu_{\text{mem}}(x, y)$ and $\mu_{\text{buf}}(x, y)$ and the numerically calculated escape times $\mu_{\text{esc}}(x, y)$ for different types of initial data and source terms, see Section 4.

We distinguished between the DHB observed for solutions with initial data given at $\mu_0 \in (-\omega_0, 0)$ and for those with initial data given at $\mu_0 \leqslant -\omega_0$. For the former ($\mu_0 \in (-\omega_0, 0)$), there are points at which the memory surface is reached before the buffer surface. We have shown examples where the entire memory surface lies below the buffer surface in 3-D, *i.e.*, $\mu_{\text{mem}}(x, y) < \mu_{\text{buf}}(x, y)$ for all (x, y) (recall the first and second representative simulations in Section 4.1). There are also examples in which only a portion of the memory surface lies below the buffer surface. In this case, $A_0(x, y)$ is such that $\mu_{\text{mem}}(x, y)$ grows with $\|(x, y)\|$ and then exceeds $\mu_{\text{buf}}(x, y)$ on some part of the domain, since ε has a small but finite value.

For the latter (where $\mu_0 \leqslant -\omega_0$), the buffer surface is reached first as μ slowly increases. That is, there are points (x, y) at which $\mu_{\text{buf}}(x, y) \leqslant \mu_{\text{mem}}(x, y)$ (noting that equality can arise when $\mu_0 = -\omega_0$). Crucially, there are two cases: (1) $\mu_{\text{buf}}(x, y) \leqslant \mu_{\text{mem}}(x, y)$ for all (x, y), and (2) $\mu_{\text{buf}}(x, y) \leqslant \mu_{\text{mem}}(x, y)$ in some regions while $\mu_{\text{mem}}(x, y) < \mu_{\text{buf}}(x, y)$ in the complementary regions. The example in Section 4.3 illustrates case (1), and an example of case (2) is given in Section 4.2. In case (2), the source term is such that it grows with $\|(x, y)\|$ and then exceeds $\mu_{\text{mem}}(x, y)$ on some part of the domain. In all simulations, we found $\mu_{\text{esc}}(x, y) \approx \min\{\mu_{\text{mem}}(x, y), \mu_{\text{buf}}(x, y)\}$.

Finally, we showed numerically that DHB occurs in the Brusselator model in two space dimensions. For several source terms $a(x, y)$, the solutions spend spatially-dependent, $\mathcal{O}(1/\varepsilon)$ long times near the repelling QSS. Also, the spatially-dependent onset of oscillations is a hard onset, as shown for

example in going from Fig. 5(e) to (f), where we note the change in scales. Moreover, after the oscillations have set in, there are dynamically complex interactions between the source term and the re-emergent component given by the initial data.

Looking ahead, we observe that it may be possible to extend the results for the CGL PDE in 2-D to include some source terms $\mathrm{I}_{\mathtt{a}}(\mathtt{x},\mathtt{y})$ that are not strictly positive or bounded. For example, in Section 8 of [18], we showed that the asymptotics for the buffer curve in the 1-D CGL PDE extend to include bounded sign-changing source terms (such as $\cos(\mathtt{x})$) and even some algebraically growing source terms (quadratic in space), and that the asymptotics still agree well with the results of numerical simulations in 1-D. Also, it may be possible to extend the results to include large-amplitude source terms and $\mathcal{O}(1)$ diffusivity, as was done for the 1-D CGL PDE in Sections 9 and 10 of [18].

We think it would be of interest to put the Brusselator PDE (35) into normal form for dynamic super-critical Hopf bifurcation, and to carry out an analysis of the linearized equation in the complex time plane similar to that done for the CGL PDE (1) in 2-D. It would be of interest to determine where the saddle points are and where the Stokes lines through them cross the real time axis, as well as to derive the homogeneous and particular solutions of the linearized equation and hence determine the spatio-temporal memory and buffer surfaces.

The spatially-dependent source terms studied here are similar to those studied in reaction-diffusion equations in two (or more) spatial variables. In [28], the authors established the conditions under which radially symmetric inhomogeneities create coherent structures, including sources, contact defects, and sinks. Also, spatial inhomogeneities have been analyzed in the Swift-Hohenberg and Ginzburg-Landau equations in 2-D in [24] and references therein. The authors demonstrate the existence of weakly-deformed stripe patterns, which are small perturbations of the uniform vertical stripes, where the small parameter measures the amplitude of the spatial inhomogeneity. While these studies are for fixed parameters, it might be of interest to study the spatio-temporal dynamics that result from the interactions between these types of heterogeneities and slow passage of a parameter through a Hopf bifurcation.

A Calculation of $A_p(x, y, \mu)$ using the saddle point method

In this appendix, we apply the saddle point method to find the asymptotic formula (7) for the particular solution $A_p(x, y, \mu)$ of the linearized CGL PDE.

In the complex $\tilde{\mu}$ plane ($\tilde{\mu} = \tilde{\mu}_R + i\tilde{\mu}_I$), the phase function in B_p is

$$\phi + i\psi = -\frac{1}{2}(\tilde{\mu} + i\omega_0)^2, \tag{40}$$

where

$$\phi = -\frac{1}{2}\left(\tilde{\mu}_R^2 - (\tilde{\mu}_I + \omega_0)^2\right) \quad \text{and} \quad \psi = -\tilde{\mu}_R(\tilde{\mu}_I + \omega_0). \tag{41}$$

This phase has a saddle point at $\tilde{\mu} = -i\omega_0$. The level sets of ϕ are hyperbolas and also known as Stokes lines. The Stokes lines with $\phi = 0$ through the saddle (which are the asymptotes of the hyperbolas) bound the valleys and hills. They may be parametrized by $\tilde{\mu}_R$ via $\tilde{\mu}_I = \pm\tilde{\mu}_R - \omega_0$. Also, the level sets of ψ are hyperbolas (with asymptotes given by the axes), and they are referred to as anti-Stokes lines.

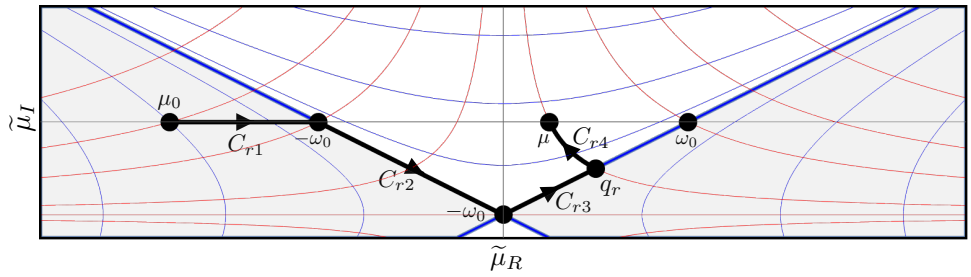

Figure 6: The contour $C_r = C_{r1} \bigcup C_{r2} \bigcup C_{r3} \bigcup C_{r4}$ in the complex $\tilde{\mu}$ plane.

Let $\delta > 0$ be a small number, independent of ε. We fix an arbitrary value of $\mu \in [\delta, \omega_0]$. We consider the contour $C_r = C_{r1} \bigcup C_{r2} \bigcup C_{r3} \bigcup C_{r4}$, where $C_{r1} = [\mu_0, -\omega_0]$; C_{r2} is the segment of the Stokes line $\tilde{\mu}_I = -\tilde{\mu}_R - \omega_0$ from $-\omega_0$ down to the saddle at $-i\omega_0$; C_{r3} is the segment of the Stokes line $\tilde{\mu}_I = \tilde{\mu}_R - \omega_0$ from the saddle up to the point $q_r = \sqrt{\omega_0\mu} + i(\sqrt{\omega_0\mu} - \omega_0)$, for this fixed value of μ; and, C_{r4} consists of the segment of the steepest ascent curve $\psi = -\omega_0\mu$ from q_r up to the point μ. See Figure 6.

We evaluate the integrals in the same manner as in Section 2.3 of [18]. We take any initial $B_p(x, y, \mu_0)$ with $\mu_0 \leqslant -\omega_0$ on or near the attracting

QSS, and we track it along C_r to the fixed value μ. At that point,

$$\begin{aligned} B_p(x,y,\mu) &= \mathcal{I}_{r1} + \mathcal{I}_{r2} + \mathcal{I}_{r3} + \mathcal{I}_{r4}, \quad \text{where for } \delta \leqslant \mu \leqslant \omega_0, \\ \mathcal{I}_{rj} &= \frac{1}{\sqrt{\varepsilon}} \int_{C_{rj}} g(x,y,\mu-\tilde{\mu}) e^{-\frac{1}{2\varepsilon}(\tilde{\mu}+i\omega_0)^2} d\tilde{\mu}, \quad j = 1,2,3,4. \end{aligned} \tag{42}$$

The integral $\mathcal{I}_{r1}$ along the segment $C_{r1} = [\mu_0, -\omega_0]$ is evaluated using the method of steepest descents along the contour formed by the union of the Stokes line through $\mu = -\mu_0$ out to $-\infty - i\omega_0$ and the Stokes line back from $-\infty - i\omega_0$ up to $\mu = -\omega_0$.n The dominant contribution comes from the final segment along the latter Stokes line near $\mu = -\omega_0$.

$$\mathcal{I}_{r1} = \left\{ \frac{\sqrt{\varepsilon}}{2\omega_0}(1+i) g(x,y,\mu+\omega_0) + \mathcal{O}\left(\varepsilon^{\frac{3}{2}}\right) \right\} e^{\frac{i\omega_0^2}{\varepsilon}}. \tag{43}$$

Next, we parametrize C_{r2} by $\tilde{\mu}_R$, with $\tilde{\mu}_I(\tilde{\mu}_R) = -(\tilde{\mu}_R + \omega_0)$, and $\tilde{\mu}_R : -\omega_0 \to 0$. Hence, $-\frac{1}{2}(\tilde{\mu} + i\omega_0)^2 = i\tilde{\mu}_R^2$ for all $\tilde{\mu}$ on C_{r2}. It is purely imaginary, corresponding to the fact that C_{r2} lies on a Stokes line $\phi = 0$. Hence, for each $\tilde{\mu}$ on C_{r2}, the integrand is of the form to which the method of stationary phase applies, namely $g \cdot e^{\frac{i}{\varepsilon} h(\tilde{\mu}_R)}$ with $h(\tilde{\mu}_R) = \tilde{\mu}_R^2$. Moreover, the end point $\tilde{\mu} = -i\omega_0$ of C_{r2} ($\tilde{\mu}_R = 0$) is a point of stationary phase, since $h'(0) = 0$ and $h''(0) = 2 \neq 0$, and it is the only such point along C_{r2}. [For the general method in which an end point is a saddle (or turning) point, see for example Section 4.1 of [35], especially formula (4.14).]

Applying the method of stationary phase, we insert the parametrization of C_{r2}, use $\tilde{\nu} = -\tilde{\mu}_R$, Taylor expand about $\tilde{\nu} = 0$ (*i.e.,* $\tilde{\mu} = -i\omega_0$), and observe that the dominant contribution asymptotically comes from the point of stationary phase at the saddle,

$$\begin{aligned} \mathcal{I}_{r2} &= \frac{1}{\sqrt{\varepsilon}} \int_{-\omega_0}^{0} g(x,y,\mu - [\tilde{\mu}_R - i(\tilde{\mu}_R + \omega_0)]) e^{\frac{i}{\varepsilon}\tilde{\mu}_R^2} (1-i) d\tilde{\mu}_R \\ &= \frac{1}{\sqrt{\varepsilon}}(1-i) \int_0^{\omega_0} g(x,y,\mu + [\tilde{\nu} + i(-\tilde{\nu} + \omega_0)]) e^{\frac{i}{\varepsilon}\tilde{\nu}^2} d\tilde{\nu} \\ &= \frac{1}{\sqrt{\varepsilon}}(1-i) g(x,y,\mu+i\omega_0) \int_0^{\omega_0} (1 + \mathcal{O}(\tilde{\nu})) e^{\frac{i}{\varepsilon}\tilde{\nu}^2} d\tilde{\nu} \\ &= \sqrt{\frac{\pi}{2h''(0)}} e^{\frac{i\pi}{4}} (1-i) g(x,y,\mu+i\omega_0) + \mathcal{O}(\sqrt{\varepsilon}) \\ &= \sqrt{\frac{\pi}{2}} g(x,y,\mu+i\omega_0) + \mathcal{O}(\sqrt{\varepsilon}), \quad \text{for any } \mu \in [\delta, \omega_0]. \end{aligned} \tag{44}$$

This leading order term in $\mathcal{I}_{r2}$ will turn out to be half of the leading order term in the total integral for $B_p(x,y,\mu)$ for each $\mu \in [\delta, \omega_0]$.

Next, we show that $\mathcal{I}_{r3}$ gives the other half of the leading order term in B_p. From the definition of C_{r3}, we have that, for any $\mu \in [\delta, \omega_0]$, $\mathcal{I}_{r3} = \frac{1}{\sqrt{\varepsilon}} \int_{-i\omega_0}^{q_r} g(x, y, \mu - \tilde{\mu}) e^{-\frac{1}{2\varepsilon}(\tilde{\mu}+i\omega_0)^2} d\tilde{\mu}$. We use $\tilde{\mu}_R$ to parametrise C_{r3} as $\tilde{\mu}_I = \tilde{\mu}_R - \omega_0$, now with $\tilde{\mu}_R : 0 \to \sqrt{\omega_0 \mu}$. Hence, $-\frac{1}{2}(\tilde{\mu}+i\omega_0)^2 = -i\tilde{\mu}_R^2$ along C_{r3}; and, for each $\tilde{\mu}$ on C_{r3}, the integral is also of the form to apply the method of stationary phase, $g \cdot e^{\frac{i}{\varepsilon}\tilde{h}(\tilde{\mu}_R)}$, with $\tilde{h}(\tilde{\mu}_R) = -\tilde{\mu}_R^2$. Moreover, the initial point $\tilde{\mu} = -i\omega_0$ of C_{r3} ($\tilde{\mu}_R = 0$) is a stationary phase point, since $\tilde{h}'(0) = 0$ and $\tilde{h}''(0) = -2 \neq 0$, and it is the only such point along C_{r3}. We find

$$\begin{aligned}
\mathcal{I}_{r3} &= \frac{1}{\sqrt{\varepsilon}} \int_0^{\sqrt{\omega_0 \mu}} g(x, y, \mu - [\tilde{\mu}_R + i(\tilde{\mu}_R - \omega_0)]) e^{-\frac{i}{\varepsilon}\tilde{\mu}_R^2} (1+i) d\tilde{\mu}_R \\
&= \frac{1}{\sqrt{\varepsilon}} g(x, y, \mu + i\omega_0) \int_0^{\sqrt{\omega_0 \mu}} e^{-\frac{i}{\varepsilon}\tilde{\mu}_R^2} (1 + \mathcal{O}(\tilde{\mu}_R))(1+i) d\tilde{\mu}_R \\
&= \sqrt{\frac{\pi}{2|\tilde{h}''(0)|}} g(x, y, \mu + i\omega_0) e^{-\frac{i\pi}{4}} (1+i) + \mathcal{O}(\sqrt{\varepsilon}) \\
&= \sqrt{\frac{\pi}{2}} g(x, y, \mu + i\omega_0) + \mathcal{O}(\sqrt{\varepsilon}), \quad \text{for any } \mu \in [\delta, \omega_0].
\end{aligned} \tag{45}$$

Finally, we calculate $\mathcal{I}_{r4}$. Implicitly parametrise C_{r4} using σ,

$$C_{r4}: \quad -\frac{1}{2}(\tilde{\mu} + i\omega_0)^2 = -\frac{1}{2}(\mu + i\omega_0)^2 + \sigma.$$

The parameter σ starts from $-\frac{1}{2}(\omega_0^2 - \mu^2)$ at the point q_r and increases monotonically along C_{r4} to zero at μ. The explicit representation is

$$\tilde{\mu}(\sigma) = -i\omega_0 + \left[(\mu + i\omega_0)^2 - 2\sigma\right]^{\frac{1}{2}}.$$

The integration along C_{r4} gives

$$\mathcal{I}_{r4} = \sqrt{\varepsilon} e^{-\frac{1}{2\varepsilon}(\mu+i\omega_0)^2} \int_{\frac{-(\omega_0^2-\mu^2)}{2}}^{0} \frac{g(x, y, \mu + i\omega_0 - [(\mu+i\omega_0)^2 - 2\sigma]^{\frac{1}{2}}) e^{\frac{\sigma}{\varepsilon}}}{\sqrt{(\mu+i\omega_0)^2 - 2\sigma}} d\sigma.$$

Hence, one finds

$$\begin{aligned}
\mathcal{I}_{r4} = \Bigg[&-\frac{\sqrt{\varepsilon} I_a(x)}{\mu + i\omega_0} + \varepsilon^{\frac{3}{2}} \left(\frac{I_a(x, y) + d(\mu + i\omega_0) \Delta I_a(x, y)}{(\mu + i\omega_0)^3} \right) \\
&+ \mathcal{O}\left(\frac{\varepsilon^{\frac{5}{2}}}{(\mu + i\omega_0)^5} \right) \Bigg] e^{-\frac{1}{2\varepsilon}(\mu+i\omega_0)^2}.
\end{aligned} \tag{46}$$

Summing (43), (44), (45), and (46), we have that, for $\delta \leqslant \mu \leqslant \omega_0$,

$$\begin{aligned} B_p(x,y,\mu) &= \mathcal{I}_{r1} + \mathcal{I}_{r2} + \mathcal{I}_{r3} + \mathcal{I}_{r4} \\ &= -\frac{\sqrt{\varepsilon} I_a(x,y)}{\mu + i\omega_0} e^{-\frac{1}{2\varepsilon}(\mu+i\omega_0)^2} \\ &\quad + \varepsilon^{\frac{3}{2}} \left(\frac{I_a(x,y) + d(\mu+i\omega_0)\Delta I_a(x,y)}{(\mu+i\omega_0)^3} \right) e^{-\frac{1}{2\varepsilon}(\mu+i\omega_0)^2} \\ &\quad + \mathcal{O}\left(\frac{\varepsilon^{\frac{5}{2}} e^{-\frac{1}{2\varepsilon}(\mu+i\omega_0)^2}}{(\mu+i\omega_0)^5} \right) \\ &\quad + \sqrt{2\pi} g(x,y,\mu+i\omega_0) + \mathcal{O}(\sqrt{\varepsilon}). \end{aligned} \tag{47}$$

Finally, we translate the formula back to the dependent variable A, completing the derivation of (7).

Acknowledgements The authors congratulate Bernd Krauskopf on the occasion of this sixtieth birthday. We are pleased to help honor his many contributions to the fields of bifurcation theory, dynamical systems, delay differential equations, numerical methods for dynamical systems, and applications of dynamical systems.

The research of the authors was partially supported by NSF-DMS 2307650 (RG). The authors thank David Barton, Andrus Giraldo, Andrew Keane, James Knowles, Hinke Osinga, and Sebastian Wieczorek for organizing the conference "Frontiers in Applied Dynamical Systems" held at the University of Cork, Ireland, June 18-20, 2024 and for editing this issue.

References

[1] I.S. Aranson and L. Kramer [2002], The world of the Complex Ginzburg-Landau equation, *Rev. Mod. Phys.*, **74**, 99–143

[2] P. Ashwin, S. Wieczorek, R. Vitolo, and P. Cox [2012], Tipping points in open systems: bifurcation, noise-induced, and rate-dependent examples in the climate system, *Phil. Trans. Roy. Soc. A*, **370**, 1166–1184

[3] D. Avitabile, M. Desroches, R. Veltz, and M. Wechselberger [2020], Local theory for spatio-temporal canards and delayed bifurcations, *SIAM J. Math. An.*, **52**, 5703–5747

[4] S.M. Baer, T. Erneux, and J. Rinzel [1989], The slow passage through a Hopf bifurcation: delay, memory effects, and resonance, *SIAM J. Appl. Math.*, **49**, 55–71

[5] E. Barreto and J.R. Cressman [2011], Ion concentration dynamics as a mechanism for neuronal bursting, *J. Biol. Phys.*, **37**, 361–373

[6] C.M. Bender and S.A. Orszag [1999], *Advanced Mathematical Methods for Scientists and Engineers: Asymptotic Methods and Perturbation Theory*, Springer-Verlag, New York

[7] I. Berenstein, M. Dolnik, A.M. Zhabotinsky, and I.R. Epstein [2003], Spatial periodic perturbation of Turing pattern development using a striped mask, *J. Phys. Chem. A*, **107**, 4428–4435

[8] F. Berthier, J.-P. Diard, and S. Nugues [1997], On the nature of the spontaneous oscillations observed for the Koper-Sluyters electrocatalytic reaction, *J. Electroanalytical Chem.*, **436**, 35–42

[9] R. Bertram, M. Butte, T. Kiemel, and A. Sherman [1995], Topological and phenomenological classification of bursting oscillations, *Bull. Math. Bio.*, **57**, 413–439

[10] L.M. Bilinsky and S. M. Baer [2018], Slow passage through a Hopf bifurcation in excitable nerve cables: Spatial delays and spatial memory effects, *Bull. Math. Bio.*, **80**, 130–150

[11] B. Braaksma [1998], Singular Hopf bifurcation in systems with fast and slow variables, *J. Nonlin. Sci.*, **8**, 457–490

[12] G. Dangelmayr and I. Oprea [2004], A bifurcation study of wave patterns for electroconvection in nematic liquid crystals, *Mol. Cryst. Liq. Cryst.*, **413**, 305–320

[13] G. Dangelmayr and I. Oprea [2008], Modulational stability of travelling waves in 2D anisotropic systems, *J. Nonlinear Sci.*, **18**, 1–56

[14] H. Engler, H.G. Kaper, T.J. Kaper, and T. Vo [2017], Dynamical systems analysis of the Maasch-Saltzman model for glacial cycles, *Physica D*, **359**, 1–20

[15] I.R. Epstein and J.A. Pojman [1998], *An Introduction to Nonlinear Chemical Dynamics: Oscillations, Waves, Patterns, and Chaos*, Oxford Univ. Press, Oxford, UK

[16] T. Erneux and E. Reiss [1990], Delaying the Transition to Hopf Bifurcation by Slowly Varying the Bifurcation Parameter, in *Spatial inhomogeneities and transient behaviour in chemical kinetics*, P. Gray, G.

Nicolis, F. Baras, P. Borckmans, and S. Scott, eds., Proc. Nonlin. Sci., Manchester University Press, Manchester, Chap. 18, 267—278

[17] P.L. Gentili and J.-C. Micheau [2020], Light and chemical oscillations: Review and perspectives, *J. Photoch. Photobio. C*, **43**, 100321

[18] R. Goh, T.J. Kaper, and T. Vo [2022], Delayed Hopf Bifurcation and Space–Time Buffer Curves in the Complex Ginzburg–Landau Equation, *IMA Journal of Applied Mathematics*, **87**, 131–186

[19] J. Grasman and J. J. Wentzel [1994], Co-existence of a limit cycle and an equilibrium in Kaldor's business cycle model and its consequences, *J. Econ. Behav. Organization*, **24**, 369–377

[20] X. Han, F. Xia, P. Ji, Q. Bi, and J. Kurths [2016], Hopf-bifurcation-delay-induced bursting patterns in a modified circuit system, *Comm. Nonlin. Sci. Num. Sim.*, **36**, 517–527

[21] M.G. Hayes, T.J. Kaper, P. Szmolyan, and M. Wechselberger [2016], Geometric desingularization of degenerate singularities in the presence of fast rotation: A new proof of known results for slow passage through Hopf bifurcations, *Indag. Math.*, **27**, 1184–1203

[22] M. Higuera, J. Porter, and E. Knobloch [2008], Faraday waves, streaming flow, and relaxation oscillations in nearly circular containers, *Chaos*, **18**, 015104

[23] L. Holden and T. Erneux [1993], Slow passage through a Hopf bifurcation: From oscillatory to steady state solutions, *SIAM J. Appl. Math.*, **53**, 1045–1058

[24] G. Jaramillo, A. Scheel, and Q. Wu [2019], The effect of impurities on striped phases, *Proc. Roy. Soc. Edin. A*, **149**, 131–168

[25] N. Kakiuchi and K. Tchizawa [1997], On an explicit duck solution and delay in the FitzHugh-Nagumo equation, *J. Diff. Eq.*, **141**, 327–339

[26] T.J. Kaper and T. Vo [2018], Delayed loss of stability due to the slow passage through Hopf bifurcations in reaction-diffusion equations, *Chaos,* **28**, 091103

[27] J. Kevorkian and J.D. Cole [1981], *Perturbation Methods in Applied Mathematics*, Applied Mathematical Sciences series, **34**, Springer, NY

[28] R. Kollar and A. Scheel [2007], Coherent structures generated by inhomogeneities in oscillatory media, *SIAM J. Appl. Dyn. Sys.*, **6**, 236–262

[29] M.T.M. Koper [1998], Nonlinear phenomena in electrochemical systems, *J. Chem. Soc. Faraday Trans.*, **94**, 1369–1378

[30] M.T.M. Koper and B.D. Aguda [1996], Experimental demonstration of delay and memory effects in the bifurcations of nickel electrodissolution, *Phys. Rev. E*, **54**, 960–963

[31] P. Kügler [2016], Early afterdepolarizations with growing amplitudes via delayed subcritical Hopf bifurcations and unstable manifolds of saddle-foci in cardiac action potential dynamics, *PLoS One*, **11**, e0151178

[32] D. Lacitignola, B. Bozzini and I. Sgura [2015], Spatio-temporal organization in a morphochemical electrodeposition model: Hopf and Turing instabilities and their interplay, *Euro. J. Appl. Math.*, **26**, 143–173

[33] K.A. Maasch and B. Saltzman [1990], A low-order dynamic model of global climate variability over the full Pleistocene, *J. Geophys. Res.*, **95**, D2: 1955–1963

[34] S. MacNamara and G. Strang [2016], Operator splitting, in *Splitting Methods in Communication, Imaging, Science, and Engineering, Scientific Computation*, 5–114, ed. R. Glowinski, S. Osher, and W. Yin, Springer International

[35] J.D. Murray [1984], *Asymptotic Analysis*, 2nd ed. Applied Mathematical Sciences series, vol. 48, Springer, New York

[36] A.I. Neishtadt [1987], Persistence of stability loss for dynamical bifurcations. I, *Diff. Urav.*, **23**, 2060–2067 (Russian). [English translation: *Diff. Eq.*, **23** (1988) 1385–1391, Plenum Pub. Corp.]

[37] A.I. Neishtadt [1988], Persistence of stability loss for dynamical bifurcations. II, *Diff. Urav.*, **24**, 226–233 (Russian). [English translation: *Diff. Eq.*, **24** (1988) 171–176, Plenum Pub. Corp.]

[38] A.I. Neishtadt [1995], On calculation of stability loss delay time for dynamical bifurcations, in *Proc. XI-th International Congress on Mathematical Physics*, 280–287, ed. Daniel Iagolnitzer, International Press, Cambridge, USA

[39] A.I. Neishtadt and V.V. Sidorenko [1997], Stability loss delay in a Ziegler system, *J. Appl. Maths. Mechs.*, **61**, 15–25

[40] A.I. Neishtadt and D.V. Treschev [2021], Dynamical phenomena connected with stability loss of equilibria and periodic trajectories, *Russ. Math. Surv.*, **76**, 883–926

[41] F. Paquin-Lefebvre. W. Nagata and M.J. Ward [2019], Pattern Formation and Oscillatory Dynamics in a 2-D Coupled Bulk-Surface Reaction-Diffusion System, *SIAM J. Appl. Dyn. Syst.*, **18**, 1334–1390

[42] I. Prigogine and R. Lefever [1968], Symmetry Breaking Instabilities in Dissipative Systems. II, *J. Chem. Phys.*, **48**, 1695–1700

[43] J. Rinzel and S. Baer [1988], Firing threshold of the Hodgkin-Huxley model for a slow current ramp: a memory effect and its dependence on fluctuations, *Biophys. J.*, **54**, 551–555

[44] J. Rubin and D. Terman [2002], Geometric singular perturbation analysis of neuronal dynamics, in *Handbook of Dynamical Systems*, B. Fiedler (ed.), **2** and **3**, Elsevier, 93–146

[45] W. van Saarloos [2003], Front propagation into unstable states, *Physics Reports*, **386**, 29–222

[46] M.A. Shishkova [1973], A discussion of a certain system of differential equations with a small parameter multiplying the highest derivatives, *Dokl. Akad. Nauk SSSR*, **209**, 576–579

[47] P. Strizhak and M. Menzinger [1996], Slow passage through a supercritical Hopf bifurcation: Time-delayed response in the Belousov-Zhabotinsky reaction in a batch reactor, *J. Chem. Phys.*, **105**, 10905

[48] J. Su [1993], Delayed oscillation phenomena in the FitzHugh Nagumo equation, *J. Diff. Eq.*, **105**, 180–215

[49] J. Su [2001] The phenomenon of delayed bifurcation and its analyses, in *Multiple-Time-Scale Dynamical Systems*, C.K.R.T. Jones and A.I. Khibnik (eds.), IMA Volumes in Mathematics and its Applications **122**, Springer, New York, 203–214

[50] H. Wu, Y. Ye, M. Chen, A. Xu, and B. Bao [2019], Extremely slow passages in a low-pass filter-based memristive oscillator, *Nonlinear Dynam.*, **97**, 2339–2353